Embedding Heterostructured α-MnS/MnO Nanoparticles in S-Doped Carbonaceous Porous Framework as High-Performance Anode for Lithium-Ion Batteries

Yuan Ma[+],[a, b] Yanjiao Ma[+],[a, b] Thomas Diemant,[c] Kecheng Cao,[d] Ute Kaiser,[d] R. Jürgen Behm,[a, c] Alberto Varzi,*[a, b] and Stefano Passerini*[a, b]

In this work, the synthesis of α-MnS/MnO/S-doped C micro-rod composites *via* a simple sulfidation process is demonstrated, starting from a Mn-based metal-organic framework. The resulting heterostructured α-MnS/MnO nanoparticles (8 ± 2 nm) are uniformly embedded into the S-doped carbonaceous porous framework with hierarchical micro-/meso-porosity. The combination of structural and compositional characteristics results in the promising electrochemical performance of the as-obtained composites as anode materials for lithium-ion batteries, coupled with high reversible capacity (940 mAh g^{-1} at 0.1 A g^{-1}), excellent rate capability as well as long cycling lifespan at high rate of 2.0 A g^{-1} for 2000 cycles with the eventual capacity of ~300 mAh g^{-1}. Importantly, *in situ* X-ray diffraction studies clearly reveal mechanistic details of the lithium storage mechanism, involving multistep conversion processes upon initial lithiation.

1. Introduction

Nowadays, the lithium-ion battery (LIB) technology is approaching its limits with regard to energy density. This is mainly caused by the commercially-used graphite-based negative electrodes, which have a relatively poor specific capacity of around 372 mAh g^{-1}.[1–3] Accordingly, the fast-growing needs of batteries especially for automotive applications, derives scientists and engineers to explore high-performance anode materials.[1,4,5]

Over the past decades, transition metal oxides (TMOs) and transition metal sulfides (TMSs) have been presented as alternative to graphite materials, due to their high theoretical specific capacities arising from conversion reactions.[6] Among them, Mn-based materials (*e.g.*, MnO and α-MnS), which feature environmental friendliness, natural abundance, and a low operating potential, are considered as appealing alternative anodes for lithium batteries.[2,7,8] However, Mn-based compounds with high capacity such as MnO and α-MnS suffer from several issues during repeated (dis-)charge processes. Specifically, severe structural variation during repeated de-/lithiation causes the short cycling lifespan, and low electronic conductivity as well as sluggish kinetics lead to poor rate capability, thus limiting their practical application.[2,7,9]

To solve these problems and achieve good lithium storage performance, various approaches have been proposed. According to our previous works,[4,10,11] the fabrication of nano/microstructured composite materials, i.e., nanoscale TMO or TMS particles uniformly anchored in a porous carbon matrix/layer, is one of the most effective methods, which can significantly relieve the mechanical stress caused by the known conversion process, and thus enhance the cycling stability. Meanwhile, the carbonaceous component in as-obtained composite enhances the electronic conductivity and prevents agglomeration of TMO or TMS nanoparticles (NPs) upon cycling.[12] In addition, the development of heterostructures has recently been confirmed to own great potential for energy storage materials, due to the synergetic physicochemical characteristics contributed by each component.[13] Specifically, the reaction kinetics, *i.e.*, the charge transfer capability, at the electrode/electrolyte interface have been significantly enhanced through such synergetic effects deriving from the improved ionic/electronic transport at the solid-solid heterojunction between two components within the electroactive material.[13–15] For instance, by investigating SnO_2/SnS-based heterostructural anode materials, Zheng et al. displayed outstanding properties with fast sodium storage kinetics and charge transport.[13] The group of Zhang synthesized a hierarchically porous MnS/MnO/C composite, presenting good performance as lithium anode with providing a specific capacity of 628 mAh g^{-1} over 330 cycles at 1 A g^{-1}.[15] Based on these

[a] Dr. Y. Ma,[+] Dr. Y. Ma,[+] Prof. Dr. R. J. Behm, Dr. A. Varzi, Prof. Dr. S. Passerini
Helmholtz Institute Ulm (HIU) Electrochemical Energy Storage,
Helmholtzstrasse 11, 89081 Ulm, Germany
E-mail: alberto.varzi@kit.edu
stefano.passerini@kit.edu
[b] Dr. Y. Ma,[+] Dr. Y. Ma,[+] Dr. A. Varzi, Prof. Dr. S. Passerini
Karlsruhe Institute of Technology (KIT),
P.O. Box 3640, 76021 Karlsruhe, Germany
[c] Dr. T. Diemant, Prof. Dr. R. J. Behm
Institute of Surface Chemistry and Catalysis, Ulm University,
Albert-Einstein-Allee 47, 89081 Ulm, Germany
[d] Dr. K. Cao, Prof. Dr. U. Kaiser
Central Facility for Electron Microscopy,
Group of Electron Microscopy of Materials Science,
Ulm University, Albert-Einstein-Allee 11, 89081 Ulm, Germany
[+] These authors contribute equally

Supporting information for this article is available on the WWW under https://doi.org/10.1002/celc.202100110

features, the design and construction of composite materials by anchoring, in particular, heterostructured α-MnS/MnO NPs in porous carbon matrices/layers appears a promising strategy to improve the lithium storage performance. Nevertheless, building such composites with diverse characteristics generally requires complicated, time-consuming, and expensive syntheses, which is difficult to scale up for practical applications. Therefore, it is necessary to search for a simple and highly efficient strategy to reduce the complexity of the synthesis procedures.

Herein, we report the facile sulfidation process to fabricate micro-rod composites consisting of heterostructured α-MnS/MnO NPs and an S-doped carbon-based porous framework (denoted as α-MnS/MnO/SCPF), starting from a Mn-based metal-organic framework (Mn–MOF) as the only precursor. Despite some progress in MOF-derived, heterostructured metal composites, the synthesis of such Mn-based composites by using MOF-driven approach is, to the best of our knowledge, reported here for the first time.[16] Herein, we systematically studied the physicochemical features and the Li-ion storage performance of the as-obtained composite. Furthermore, the electrochemical behavior of α-MnS/MnO/SCPF-based electrodes was systematically investigated by using *in situ* X-ray diffraction (XRD) measurement.

2. Results and Discussion

The formation of the α-MnS/MnO/SCPF composites is schematically illustrated in Figure 1a. Employing Mn–MOFs as precursors, α-MnS/MnO/SCPF composites were prepared by an efficient strategy in a simultaneous annealing and sulfidation process. The well-defined Mn–MOF micro-rods were prepared *via* a simple method, which is described in more detail in our previous study.[17] The as-obtained Mn–MOF precursor is transformed into α-MnS/MnO/SCPF *via* the facile sulfidation reaction (detailed description in the Experimental Section). Upon the sulfidation process, Mn-ions in the MOF react with sulfur vapor

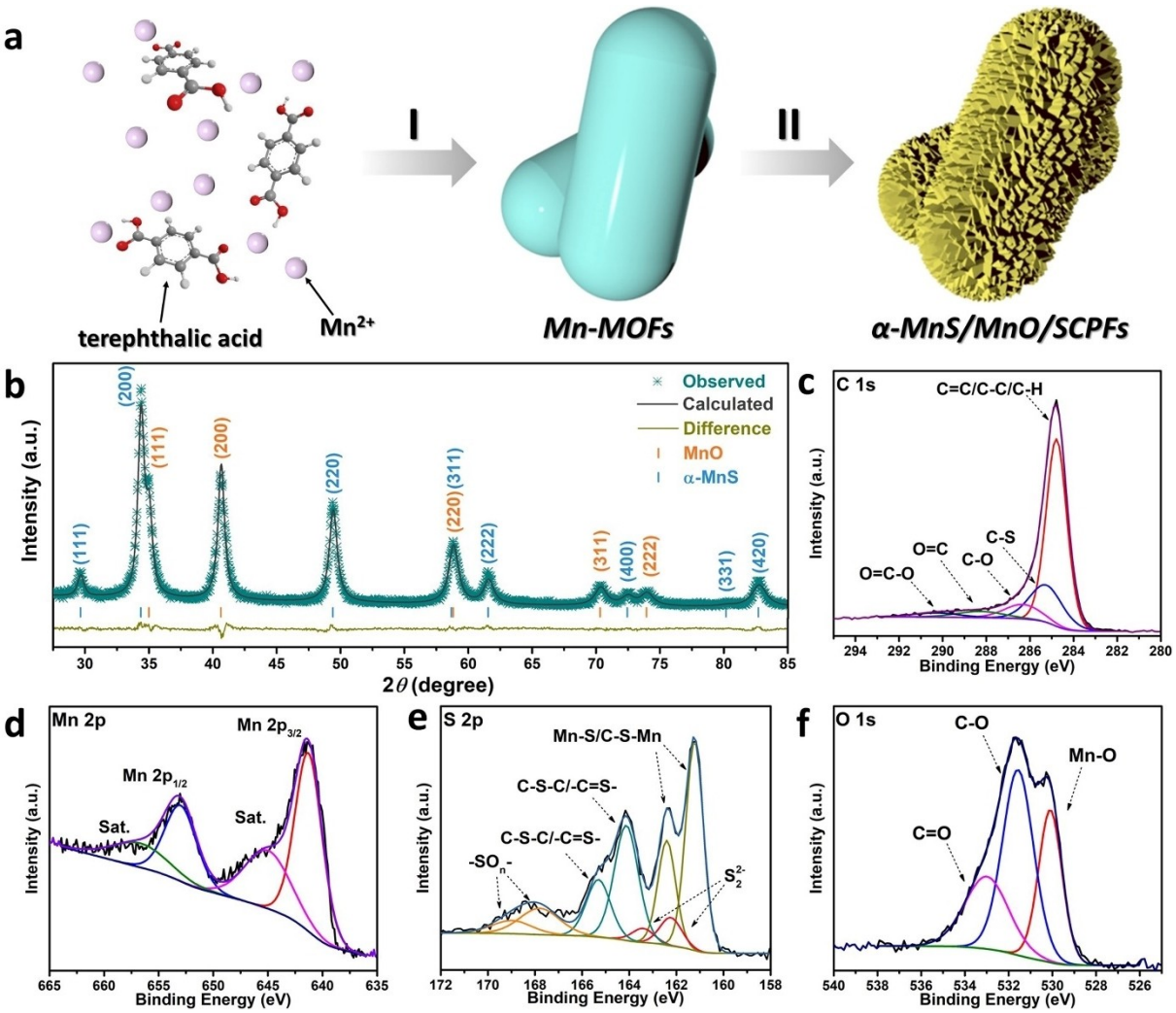

Figure 1. a) Schematic description of the synthesis procedure of α-MnS/MnO/SCPF composites. b) Powder XRD diffractions of α-MnS/MnO/SCPF and related Rietveld refinement analysis. Observed, calculated, and difference patterns are shown in cyan, black, and yellow, respectively. The vertical ticks indicate the expected Bragg positions for both α-MnS (blue ticks) and MnO (orange ticks). c-f) XPS spectra of c) C 1s, d) Mn 2p, e) S 2p, and f) O 1s for the as-prepared α-MnS/MnO/SCPF.

and/or with oxygen (from the organic ligands), yielding uniform α-MnS and MnO nanoparticles.[17,18] Meanwhile, the organic ligands are *in situ* carbonized and sulfidated, yielding to the whole MOF structure being transformed into a porous carbonaceous framework.[17–19]

Figure 1b shows the powder XRD diffractogram with the Rietveld refinement analysis of α-MnS/MnO/SCPF, demonstrating that the composite is a mixture of cubic α-MnS (Fm-3 m space group with $a=b=c=5.216(5)$ Å) and cubic MnO (Fm-3 m space group with $a=b=c=4.438(4)$ Å) with the relative weight fractions being 51% and 49%, respectively. Note that the Rietveld refinement analysis was conducted with acceptable agreement factors ($R_{wp}=10.82\%$, $R_p=7.53\%$) (ICSD α-MnS: 41331, MnO: 9864). In addition, other significant reflections resulting from impurities are not seen in the XRD pattern.

X-ray photoelectron spectroscopy (XPS) was used to study the surface properties of α-MnS/MnO/SCPF, identifying its chemical composition and the presence of specific functional groups. The survey spectrum (see Figure S1) demonstrates that only the four elements C, O, S, and Mn are present in the as-obtained composite material. Figure 1c displays the C 1s core-level XPS spectrum, which consists of five peaks centered at binding energies of 284.8, 285.2, 286.3, 288.3, and 290.3 eV, which can be ascribed to C=C/C–C/C–H, C–S, C–O, C=O and O=C-O groups, respectively. This suggests that the surface of the porous carbon-based frameworks has sulfur- and oxygen-containing functional groups.[10,17] The detail spectrum of the Mn 2p region is shown in Figure 1d. The two main peaks at 641.3 (Mn $2p_{3/2}$) and 653.0 eV (Mn $2p_{1/2}$), which appear together with two satellite-peaks centered at 645.0 and 656.7 eV, suggest the existence of Mn(II) in the final product.[2,20] The chemical environment of Mn was further investigated via analysis of the Mn 3 s detail XPS spectrum (Figure S2), since the splitting of the Mn 3 s peak, arising from the interaction of the core hole with the unpaired 3 d electron(s), can be employed to identify the Mn oxidation state.[17,21] This splitting grows from ~4.7 eV for Mn^{4+} via ~5.3 eV for Mn^{3+} to ~6.0 eV for Mn^{2+}.[17,21] In the present case, the splitting is 6.0 eV for α-MnS/MnO/SCPF, pointing to a predominance of Mn^{2+} species. As shown in Figure 1e, several S species can be identified in the S 2p detail spectrum. The first doublet with peaks at 161.2 and 162.4 eV is attributed to the S $2p_{3/2}$ and S $2p_{1/2}$ peaks of Mn–S (see also Experimental Section). The second one (at 162.2 and 163.4 eV), showing a much lower intensity, is probably related to the presence of a small amount of disulfide (S_2^{2-}) species. C–S–C/–C=S functionalities are responsible for the third peak doublet at 164.1 and 165.3 eV. Finally, another relatively broad doublet is detected at higher binding energies (at 167.8 and 169.0 eV), which represents oxidized species (sulfates, etc.) presumably formed upon sample oxidation. Overall, the results indicate that the S atoms have been incorporated into the porous carbonaceous framework, along with the formation of α-MnS.[2,4,22] Finally, the O 1s detail spectrum (Figure 1f) can be fitted by three components centered at 530.1, 531.6, and 533.0 eV, which correspond to oxygen in MnO, C–O and C=O/O–C=O groups in the composite, respectively.[10,23,24]

Based on the XRD and XPS data, the Mn–MOFs precursors were successfully transformed *via* the simple reaction process into α-MnS/MnO with S-doped carbonaceous framework, containing some S- or O-containing functional groups to offer additional lithium storage sites. Notably, thermogravimetric analysis (TGA, Figure S3) shows the α-MnS, MnO, and C content to be around 23.3 wt%, 22.4 wt%, and 54.3 wt%, respectively.

Detailed morphologies and microstructures of the α-MnS/MnO/SCPF composites was obtained by scanning electron microscopy (SEM), transmission electron microscopy (TEM) and high-resolution TEM (HRTEM). The SEM image (Figure 2a) reveals that the as-obtained product consists of uniform micro-rods with lengths ranging from 2 to 4 μm and widths of about 1 μm. The morphology of α-MnS/MnO/SCPF is similar to that of the parental compounds (*i.e.*, Mn–MOFs), which apparently is retained after the sulfidation process. The close-up SEM images (Figure 2b–c) show that the surface of the α-MnS/MnO/SCPF micro-rods is rather rough. In the TEM image (Figure 2d), some α-MnS/MnO/SCPF micro-rods are overlayed on top of each other, displaying porous structural characteristics. Most likely, this stems from the formation of gaseous products such as CO_2, H_2O, and CO, which escape from the inner part of the Mn–MOF precursors upon the sulfidation procedure.[10,25] As demonstrated by the magnified TEM image in Figure 2e, the metal oxide/sulfide NPs (average grain size of 8 ± 2 nm) are highly distributed, but not agglomerated, in the porous carbonaceous framework of the micro-rods. HRTEM micrograph (Figure 2f) displays an α-MnS NP anchored in the obtained amorphous carbon layered matrix. The lattice fringes of the embedded NP with a d-spacing of 0.26 nm (Figure 2i) relate to the (200) crystalline plane of α-MnS (JCPDS card no. 88–2223). And, α-MnS/MnO NPs can also be found in the carbonaceous matrix (Figure 2g), with interlayer distances of about 0.22 nm and 0.26 nm (Figure 2h), respectively, which can be assigned to both the (200) plane of cubic MnO (JCPDS card no. 75–0625) and cubic α-MnS. Interestingly, the HRTEM image of the composite material in Figure 2h exhibits a junction region, demonstrating the formation of α-MnS/MnO heterostructures.[13,14] Furthermore, the energy-dispersive X-ray (EDX) spectroscopy elemental mapping results (Figure S4) demonstrate a uniform dispersion of C, S, O, and Mn in the α-MnS/MnO/SCPF micro-rods, confirming a rather uniform co-existence of α-MnS, MnO and S-doped carbonaceous frameworks in the composite.

The Raman spectrum of α-MnS/MnO/SCPF (see Figure S5) shows two bands at 1335 and 1589 cm^{-1} corresponding to the typical D and G bands of amorphous carbon, respectively.[10,17] In addition, N_2 adsorption-desorption isotherms (Figure S6a) reveal that the specific Brunauer-Emmett-Teller (BET) surface area of the final product is 96.2 $m^2 g^{-1}$. Importantly, by employing Barrett-Joyner-Halenda (BJH) analysis (Figure S6b), the pore-size is determined mainly located at ~1.9 nm and 2–7 nm, suggesting a hierarchical pore structure in α-MnS/MnO/SCPF, with micro- and mesopores.[25,26]

In the next step, the electrochemical performance of the α-MnS/MnO/SCPF composite material was investigated in Li half-cells in the voltage range of 0.01–3.0 V, *i.e.*, using Li metal as a

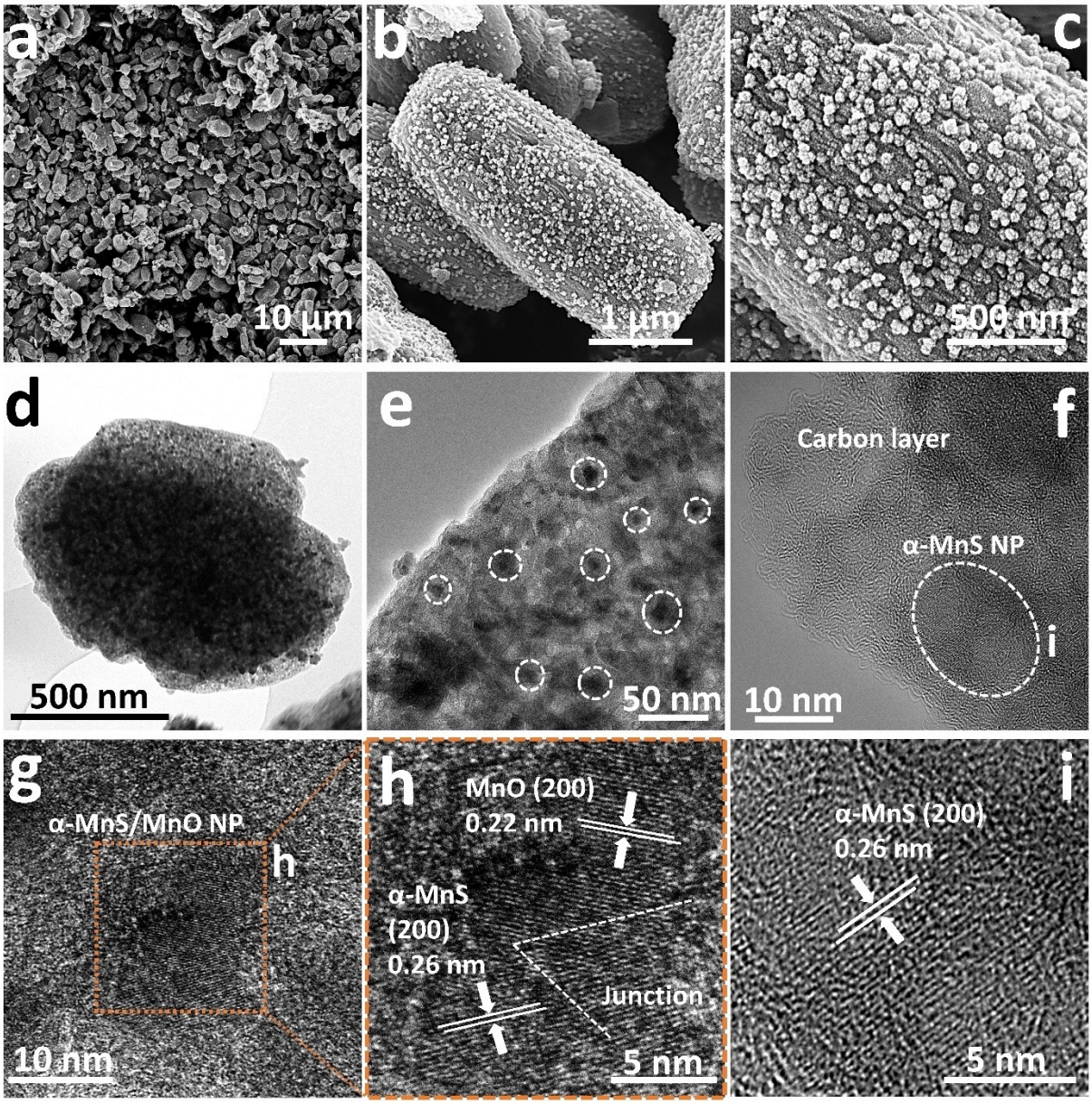

Figure 2. a-c) SEM, d-e) TEM, and f-i) HRTEM micrographs of α-MnS/MnO/SCPF micro-rods at different magnifications. The HRTEM micrographs in h) and i) are magnifications of the areas delimited by the orange rectangle in panel g) and the white ellipse in panel f), respectively.

counter electrode. Note that the weight of carbonaceous component (i.e., SCPF) is also included in the active material mass of α-MnS/MnO/SCPF-based electrode. First, the Li-ion storage process for α-MnS/MnO/SCPF is discussed. Figure 3a displays the cyclic voltammetry (CV) curves of the α-MnS/MnO/SCPF-based electrode during the first six cycles. In the first cathodic scan, a tiny feature centered at *ca.* 1.21 V is attributed to the conversion reaction of trace MnO_x ($1 < x \leq 2$), forming MnO and Li_2O.[27,28] Note that no signals of MnO_x ($1 < x \leq 2$) were found in the XRD pattern and XPS results, probably owing to its low concentration and/or amorphous nature. Subsequently, a distinct peak appeared at *ca.* 0.51 V accompanied by a shoulder, assigned to the reduction of α-MnS to Mn^0 and Li_2S, and MnO_x ($1 < x \leq 2$) to form MnO and Li_2O, as well as the generation of the solid-electrolyte interphase (SEI) layer.[9,17,27] A sharp reduction peak centered at 0.22 V is attributed to the SEI generation on MnO particles, coupled with the reduction of MnO to metallic Mn and Li_2O.[9,29] The last cathodic peak appearing at 0.01 V is assigned to Li-ion insertion into the carbon framework (including the conductive additive, *i.e.*, SuperC 65).[4,10] In the following anodic sweep, the intense feature at *ca.* 1.18 V is attributed to the re-conversion of Mn^0 to metal oxide and sulfide species.[9,17,29] Additionally, the cathodic peak at 1.69 V and the anodic peaks at 1.89 V and 2.35 V, respectively (marked in red), are ascribed to the decomposition/formation of CuS. These processes result from side reactions involving the Cu current collector, which have already been reported in our recent work.[17] The CuS formation is simply identified using a

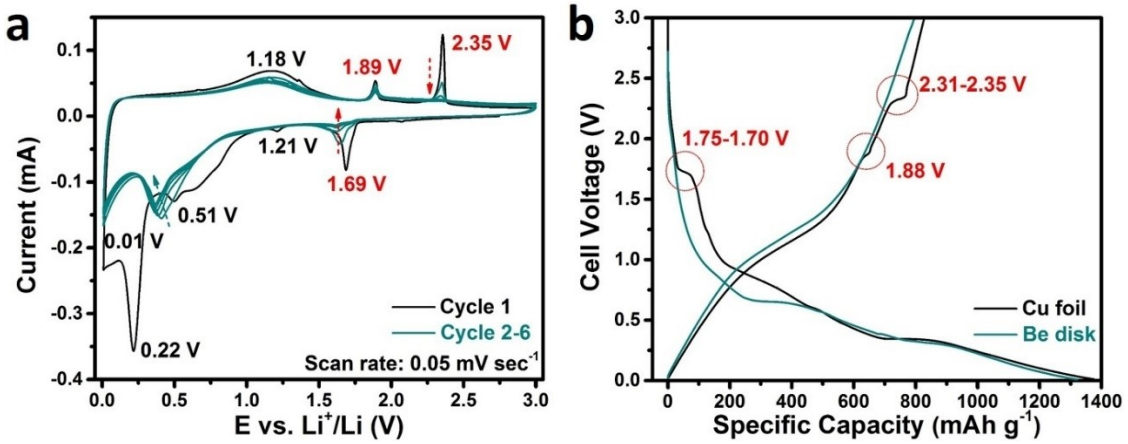

Figure 3. a) Cyclic voltammetry curves recorded during the first six cycles between 0.01 V and 3.0 V (scan rate: 0.05 mV sec^{-1}); b) comparison of the first cycle voltage profiles of electrodes with Cu foil or Be disk current collectors at a current density of 40 mA g^{-1}.

different current collector, *e.g.*, Be instead of Cu. The comparison of the first galvanostatic lithiation/de-lithiation cycle using the two different current collectors is shown in Figure 3b. Generally, the two voltage profiles exhibit similar characteristics, but three features, marked by red circles, only appear when applying Cu foil as the current collector. In line with the CV results, these features include a plateau at *ca.* 1.72 V during lithiation and two others at 1.88 V and 2.32 V during the subsequent de-lithiation, supporting the formation of CuS when coating the active material on Cu foil, and its following conversion during the de-/lithiation process. Remarkably, only rather minor modifications occur in the CV experiments (Figure 3a), *i.e.*, two CV peaks associated to CuS (1.69 V and 2.35 V) gradually disappear upon further cycling (Figure 3a) while the reduction peak at ~0.4 V exhibits a slight shift to *ca.* 0.35 V, underlining the excellent reversibility of α-MnS/MnO/SCPF.[4]

In order to well study the lithium storage process of α-MnS/MnO/SCPF, *in situ* XRD measurements were conducted during the 1st cycle of the de-/lithiation process. Figure 4a displays the evolution of the XRD patterns (97 scans, left panel) coupled with the correlated discharge/charge profile (right panel). According to the dynamic evolution of phases in XRD patterns

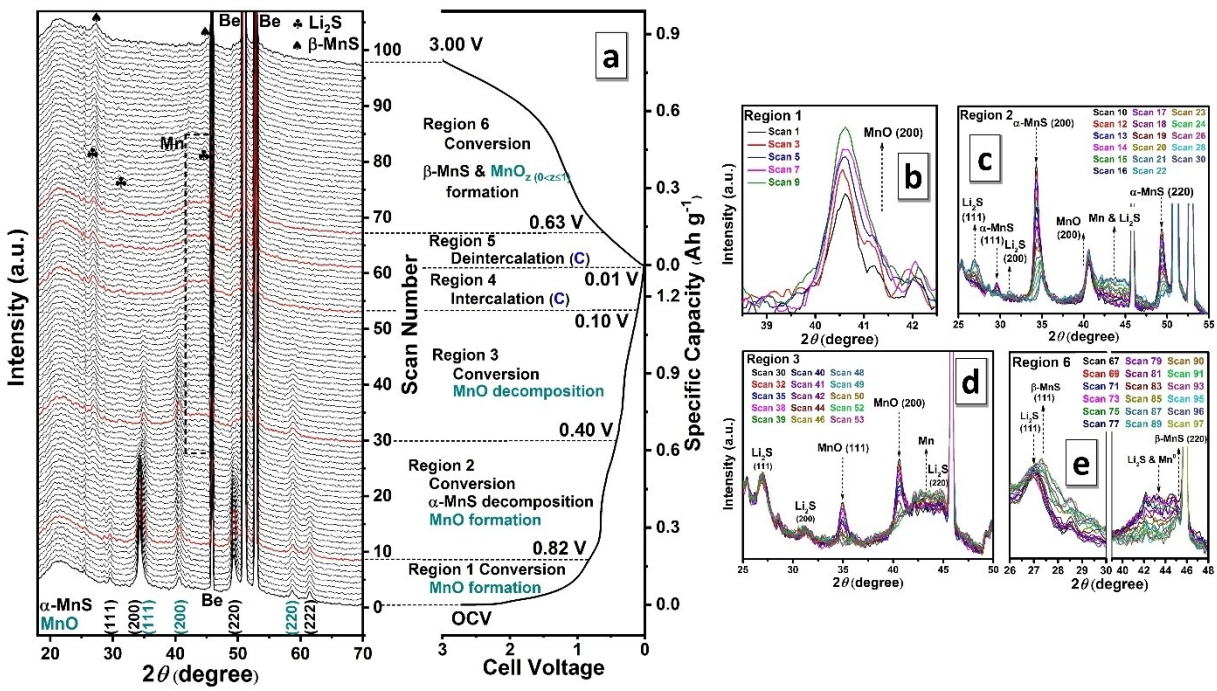

Figure 4. *In situ* XRD analysis of the α-MnS/MnO/SCPF material (coated on a Be disk acting as current collector) during galvanostatic (dis-)charge performed using an in-house-designed, two-electrode cell featuring lithium metal as counter electrode. a) As-collected XRD patterns (scans 1 to 97; left panel) coupled with corresponding initial discharge/charge profile (right panel). b–e) Close-up XRD patterns at selected areas based on the different electrochemical behavior.

combined with CV results (Figure 3a), the voltage - capacity profile contains six different regions, separately correlated to dissimilar electrochemical reactions, which are indicated by the red XRD patterns in the left panel of Figure 4a. Region 1 includes the initial potential decrease from the open-circuit voltage (OCV) to 0.82 V. The evolution of the XRD patterns in this region shows that the intensity of the MnO-related reflection of the (200) plane gradually increases, *i.e.*, the peak located at *ca.* 40.6°, which is better visible in the enlarged XRD patterns between 38° to 43° of region 1 (Figure 4b). This variation is due to the decomposition of MnO_x ($1 < x \leq 2$), gradually forming MnO and Li_2O, correlating to the CV peak at 1.21 V in the initial cathodic curve (Figure 3a).[27] The discharge profile in region 2 (voltage range from 0.82 to 0.40 V) consists of an obvious plateau (Figure 4a, right panel), corresponding to the cathodic peak at *ca.* 0.51 V in the CV cycle (Figure 3a). The XRD patterns in region 2 (scans 10 to 30 in Figure 4c) show the clear intensity decrease of the α-MnS-related reflections (*i.e.*, (200) and (220) plane) till their complete disappearance. At the same time, new reflections of Li_2S (JCPDS card no. 23-0369) and metallic Mn (JCPDS card no. 33-0887) appear, gradually gaining intensity. These results indicate that the conversion reaction of α-MnS takes place in region 2, which is again in line with the CV data.[17] Meanwhile, the intensity of the MnO-related peak at 40.6° continuously increases, suggesting for the ongoing decomposition of MnO_x species in region 2.[27] In the next region, the voltage profile shows the second main plateau from 0.4 V to 0.1 V, which correlates to the distinct CV peak at 0.22 V in the 1st CV cycle (Figure 3a). The reflections of MnO gradually decrease in intensity to disappear in scan 52, suggesting that the full decomposition of MnO occurs in region 3 (Figure 4d). Simultaneously, the features associated with metallic Mn expectedly increase. Region 4, including the full lithiation to 0.01 V, correlates to the cathodic feature at 0.01 V in the CV cycle (Figure 3a). It is well-known that Li-ions intercalation into the graphitic carbon occurs in this voltage range.[4,30] However, this process cannot be resolved in the XRD measurements due to the mostly amorphous character of the carbon matrix.[17]

Upon the subsequent delithiation process, the capacity obtained from 0.01 V to 0.63 V (region 5) originates from Li de-insertion reaction from graphitic carbon.[4,30] Increasing the potential further to 3 V, an obvious plateau appeared at ~1.2 V for the voltage - capacity profile, followed by the appearance of a slope feature that correlates to the anodic peak at about 1.18 V in the CV sweep. The corresponding XRD patterns (scans 67 to 97, Figure 4e) present an intensity decrease of the peaks assigned to metallic Mn and Li_2S, while two new peaks appeared at 27.3° and 45.6°. They suggest the formation of β-MnS (JCPDS card no. 40–1288), which reveals the conversion reaction of Mn^0 to β-MnS.[17] Finally, no reflections related to the manganese oxides are observed in the last region. It may be speculated that the oxides obtained upon charging have a (quasi-)amorphous structure.[10] This is backed by a previous x-ray absorption near edge structure (XANES) study, which showed the recovery of MnO_z ($0 < z \leq 1$) species after complete delithiation to 3.0 V.[27] Thus, we propose that the specific capacity in region 6 might at least in part originate from the re-conversion process of Mn^0 to manganese oxides (*e.g.*, MnO_z, $0 < z \leq 1$).

Based on the results of the above discussion, the initial cycle de-/lithiation mechanism of α-MnS/MnO/SCPF can be summarized as follows:

Region 1 (OCV–0.82 V) [Eqs. (1), (2)]: decomposition of MnO_x ($1 < x \leq 2$) (and CuS conversion if applying Cu foil as current collector)

$$MnO_{x\ (1<x\leq 2)} + 2(x\text{-}1)Li^+ + 2(x\text{-}1)e^- \rightarrow MnO + (x\text{-}1)Li_2O \quad (1)$$

$$(CuS + 2Li^+ + 2e^- \rightarrow Cu^0 + Li_2S) \quad (2)$$

Region 2 (0.82–0.40 V) [Eqs. (3), (4)]: α-MnS conversion, further decomposition of MnO_x ($1 < x \leq 2$)

$$MnO_{x\ (1<x\leq 2)} + 2(x\text{-}1)Li^+ + 2(x\text{-}1)e^- \rightarrow MnO + (x\text{-}1)Li_2O \quad (3)$$

$$\alpha\text{-}MnS + 2Li^+ + 2e^- \rightarrow Mn^0 + Li_2S \quad (4)$$

Region 3 (0.40–0.1 V) [Eq. (5)]: MnO conversion

$$MnO + 2Li^+ + 2e^- \rightarrow Mn^0 + Li_2O \quad (5)$$

Region 4 (0.1 - 0.01 V) [Eq. (6)]: Li intercalation in graphitic carbon

$$C_6 + yLi^+ + ye^- \rightarrow Li_yC_6 \quad (6)$$

Region 5 (0.0–0.63 V) [[Eq. (7)]: Li de-intercalation from graphitic carbon

$$Li_yC_6 \rightarrow C_6 + yLi^+ + ye^-) \quad (7)$$

Region 6 (0.63–3.0 V) [Eqs. (8)–(10)]: formation of β-MnS and $MnO_{z\ (0<z\leq 1)}$ (and CuS re-conversion if employing Cu foil as current collector)

$$Mn^0 + Li_2S \rightarrow \beta\text{-}MnS + 2Li^+ + 2e^- \quad (8)$$

$$Mn^0 + zLi_2O \rightarrow MnO_{z\ (0<z\leq 1)} + 2zLi^+ + 2ze^- \quad (9)$$

$$(Cu^0 + Li_2S \rightarrow CuS + 2Li^+ + 2e^-) \quad (10)$$

Figure 5 exhibits the electrochemical performance of α-MnS/MnO/SCPF-based electrodes as LIBs anode. For comparison purposes, α-MnS/MnO based electrodes, consisting of the simple mixture of pure (commercial) α-MnS and MnO in the weight ratio of 51:49. were evaluated as well. Figure 5a and S7 show the cycling performance of the α-MnS/MnO/SCPF and α-MnS/MnO based electrodes upon galvanostatic cycling at 40 mA g^{-1} (1st cycle) and 100 mA g^{-1} (2nd–200th cycle). For the α-MnS/MnO/SCPF-based electrodes, the values of specific capacity are referred to the mass of the whole composite, including the SCPF fraction. The α-MnS/MnO/SCPF-based electrode exhibits a high reversible capacity of 850 mAh g^{-1} in the first cycle, although the corresponding Coulombic efficiency (61%) is

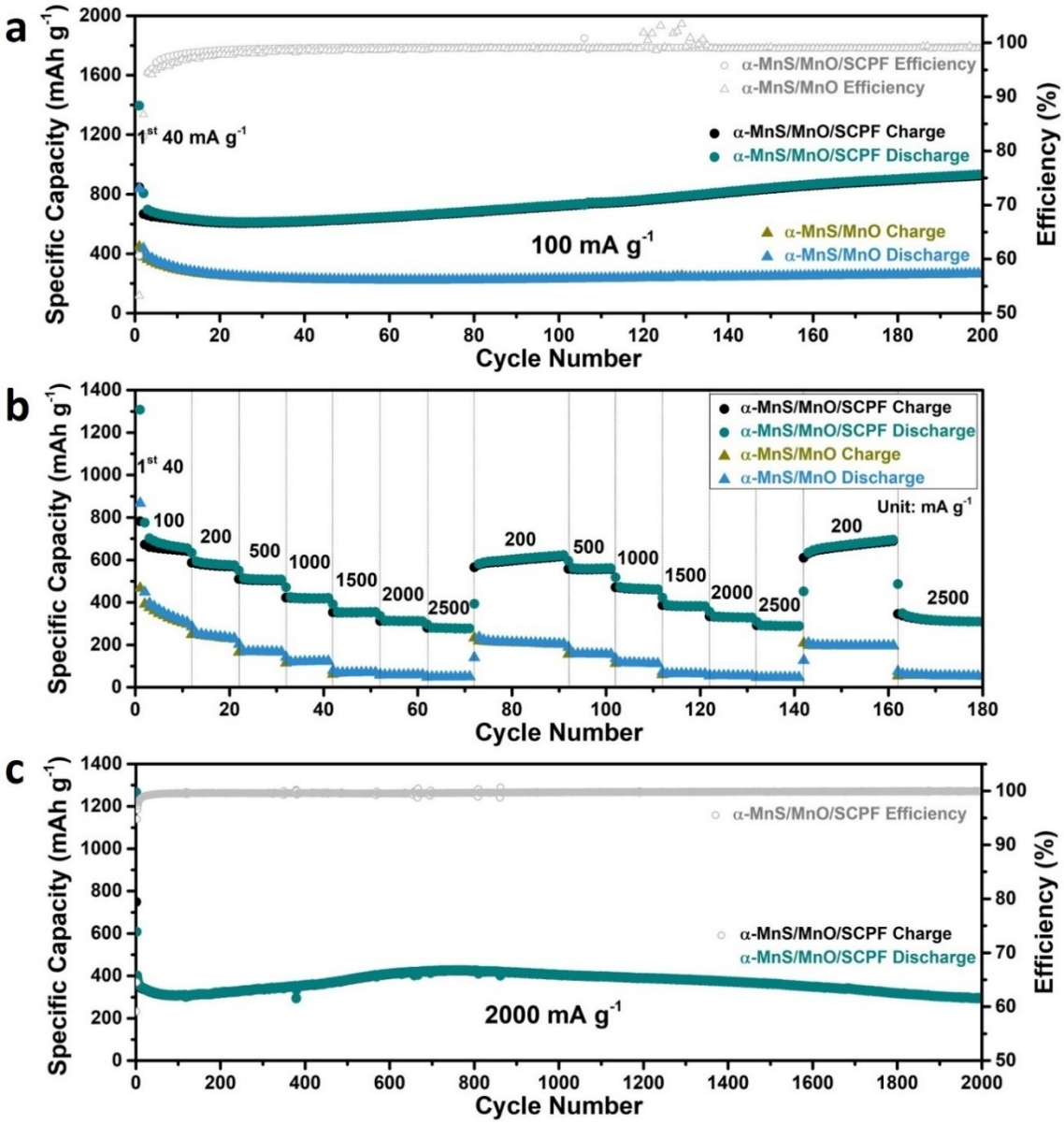

Figure 5. a) Cycling performance of α-MnS/MnO/SCPF and α-MnS/MnO (40 mA g^{-1} for initial cycle and 100 mA g^{-1} for the 2nd to 200th cycle); b) rate performance of α-MnS/MnO/SCPF and α-MnS/MnO at different current densities from 100 to 2500 mA g^{-1}; c) long-term cycling performance of the α-MnS/MnO/SCPF based electrode at a specific current of 2000 mA g^{-1}.

relatively low. This is associated with the SEI generation and the partially irreversible conversion processes (Figure S7a).[10] However, the 1st charge capacity of α-MnS/MnO/SCPF is substantially larger than that of α-MnS/MnO (446 mAh g^{-1}) and even larger than the theoretical capacity of each component (α-MnS: 616 mAh g^{-1} and MnO: 756 mAh g^{-1}). This finding can be explained by the large surface area of the active material α-MnS/MnO/SCPF nanoparticles (diameter of 8 ± 2 nm) and the S-doped carbon matrix (e.g., S- or O-containing functional groups) providing additional electrochemical active sites.[17,31–33] Furthermore, from the 2nd cycle on, the α-MnS/MnO/SCPF electrode exhibits excellent reversibility, better than the α-MnS/MnO electrode, as it is evident from the almost overlapping voltage profiles (Figure S7). The α-MnS/MnO/SCPF electrode exhibits relatively stable reversible capacities of around 610 mAh g^{-1} in the initial twenty cycles, which progressively grows afterward to finally reach *ca.* 940 mAh g^{-1} at the 200th cycle (Figure 5a). Such a capacity growth upon cycling is certainly assigned to the "quasi-reversible" formation of the SEI, which commonly exists in conversion-type materials.[17,34] Importantly, the ex-situ SEM micrograph of an electrode collected at 200th cycle (Figure S8) reveals that the α-MnS/MnO/SCPF maintains its original micro-rod morphology quite well. Apparently, the porous carbonaceous framework and the hierarchical porosity can effectively buffer the effect of active material volume expansion.[10,17]

Afterward, the α-MnS/MnO/SCPF-based and α-MnS/MnO-based electrode were both investigated by gradually increasing

the applied specific current from 0.1 to 2.5 A g^{-1}, as shown in Figures 5b and S9. The α-MnS/MnO/SCPF shows an outstanding rate capability at all applied specific currents. Specific capacities of 680, 586, 510, and 422 mAh g^{-1} are obtained for the applied specific currents of 0.1, 0.2, 0.5, and 1.0 A g^{-1}, respectively. Even at higher specific currents (*i.e.*, 1.5, 2.0 and 2.5 A g^{-1}) the electrode still delivers high average specific capacities of 354, 314 and 280 mAh g^{-1}, respectively. When the current density recovered to 0.2 A g^{-1}, the electrode shows an excellent capacity recovery (*ca.* 623 mAh g^{-1}). Importantly, α-MnS/MnO/SCPF also keeps its good rate performance upon the second time C-rate test. Notably, when the specific current was once again reduced to 200 mA g^{-1}, α-MnS/MnO/SCPF electrode still provides a high reversible capacity of ~700 mAh g^{-1} in the 161st cycle, suggesting the highly cycling reversibility. In contrast, α-MnS/MnO displays substantially inferior performance (see Figure 5b and S9b), i.e., 120 and 59 mAh g^{-1} at 1.0 and 2.0 A g^{-1} in the 1st rate capability test, and 64 and 47 mAh g^{-1} at 1.5 and 2.5 mA g^{-1} in the second one.

Looking at the voltage - capacity profiles of the obtained samples in the 1st C-rate measurement (Figure S9), the increasing overpotential recorded for α-MnS/MnO based electrode is certainly the cause of the steadily decreasing specific capacity upon the C rate test. Whereas this is much less pronounced in the α-MnS/MnO/SCPF based electrode. More precisely, a rather slowly and moderate change of the IR (internal resistance) can be observed for this cell, which results in the excellent rate capability and cycling stability.[35] The significantly improved rate performance can be ascribed to the synergetic enhancement of the Li-ion and electron transport, benefiting from the nanoscale α-MnS/MnO particles with the heterostructure as well as the C component.[10,13] The electrochemical impedance spectroscopy (EIS) further demonstrates the different kinetics between the α-MnS/MnO/SCPF-based and α-MnS/MnO-based electrodes. Both EIS profiles recorded in Figure S10 display a semicircle in the high frequency followed by a single line in the low frequency region. Note that the semicircle recorded for α-MnS/MnO is much larger than that for α-MnS/MnO/SCPF, indicating a lower impedance of the latter and further confirming the substantially enhanced Li-ion and electron transport within the as-fabricated composite material (i.e., α-MnS/MnO/SCPF).[13,16]

Finally, the long-term cycling performance of α-MnS/MnO/SCPF was tested at the high current density of 2.0 A g^{-1} (Figure 5c). Even at this high current density, the α-MnS/MnO/SCPF-based electrode presents stable long-term behavior over 2000 cycles, together with a high coulombic efficiency, reaching up to 99.5% from the ~20th to 2000th cycles. After 2000 cycles, the reversible capacity still remains about 300 mAh g^{-1}. Compared with the previous studies on α-MnS-based and/or MnO-based anode materials, α-MnS/MnO/SCPF displays a promising lithium storage performance, as summarized in Table S1.

3. Conclusions

In summary, we have successfully developed an effective and simple synthesis procedure for fabricating hierarchical porous micro-rods composed of heterostructured α-MnS/MnO nanoparticles and S-doped carbonaceous frameworks, using a Mn–MOF as the only precursor. The as-obtained composite possesses a multitude of advanced structural features, such as nanoscale α-MnS/MnO particles (of ~8 nm in diameter) with heterostructure, which are uniformly embedded in the S-doped carbonaceous matrix. Benefitting from its structural and compositional features, the resulting composite, α-MnS/MnO/SCPF, presents an excellent rate capability and outstanding cycling stability (~300 mAh g^{-1} after 2000 cycles under 2 A g^{-1}), underlining its suitability as an anode for LIBs. By *in situ* XRD analysis, we could elucidate details of the lithium storage process, involving multi-step conversion processes. Furthermore, comparison of measurements with different metals as current collector revealed the formation of CuS when casting the electrode on Cu foil. The excellent lithium storage performance and the simple MOF-driven approach render α-MnS/MnO/SCPF a promising conversion-type material for applications in energy storage techniques.

Experimental Section

Preparation of α-MnS/MnO/SCPF

First, Mn–MOF was mixed with sulfur powder (S-powder, 99.98%, Sigma-Aldrich Chemical Co.) in the 1:1 weight ratio, and the synthesis of the Mn–MOF has been reported previously.[17] Then, the as-prepared mixture was calcined under nitrogen flow at 600 °C for 2 h (5 °C min^{-1} heating rate). Finally, the black powder, α-MnS/MnO/SCPF, was obtained after naturally cooling down to room temperature.

Materials characterization

The crystalline structure of the as-obtained α-MnS/MnO/SCPF was characterized by XRD using a Bruker D8 Advance instrument (Cu-K_α radiation with a wavelength of 0.154 nm). SEM and EDX spectroscopy were performed on a ZEISS 1550VP. More morphological and microstructural information of α-MnS/MnO/SCPF micro-rods was obtained from TEM (JEOL JEM-3000) and HRTEM (C_s-corrected transmission electron microscope FEI Titan 80–300, at 80 kV). The XPS measurements on the as-prepared samples were performed on a PHI 5800 MultiTechnique ESCA System, using monochromatized Al-K_α (1486.6 eV) radiation (250 W, 13 kV), a detection angle of 45° and pass energies of 93.9 ads 29.35 eV for survey and detail spectra, respectively. The calibration for all spectra were performed according to the C1s peak of adventitious carbon at 284.8 eV. Peak fitting of the XPS spectra was done using a Shirley background and peaks based on a Gaussian-Lorentzian mix function. For the fit of the 2p spectra of S and Mn, the expected peak intensity ratio (2:1) and spin-orbit splitting (S2p = 1.2 eV, Mn2p = 11.7 eV) were fixed.[36] N_2 absorption-desorption isotherms of α-MnS/MnO/SCPF was performed on Autosorb-iQ (Quantachrome) at 77 K to obtain its specific BET surface area, and the pore size distribution based on BJH method. TGA measurements of α-MnS/MnO/SCPF were performed using a thermogravimetric analyzer (TA Instruments,

Model Q5000) with a heating rate of 5 °C min^{-1} in air. Finally, Raman spectrum of resulting product was obtained from a confocal InVia Raman microspectrometer (from Renishaw) with a 633 nm laser.

Electrochemical measurements

The working electrodes (WE) for α-MnS/MnO/SCPF and pure α-MnS/MnO (pure α-MnS: 51 wt% and pure MnO: 49 wt%; both from Alfa Aesar Chemical Co.) were composed of the active materials, conductive carbon (SuperC65, TIMCAL), and binder (polyvinylidene fluoride (PVdF)) in a weight ratio of 80:10:10. For the preparation of the WE, PVdF powder was first dissolved in *N*-methylpyrrolidinone (NMP, Sigma-Aldrich) to get a 10 wt.% solution. Then, the black powders of active material and SuperC65 were added into the obtained solution, which was then mixed by magnetic stirring overnight. As-prepared homogeneous black slurry was spread onto a copper foil (SCHLENK, 99.9%), As-obtained electrodes were first dried in an oven at 60 °C overnight, subsequently punched into disks with 12 mm diameter and vacuum-dried for 24 h at 80 °C. The active material mass loading of each disk electrode (α-MnS/MnO/SCPF or α-MnS/MnO) was 1.4-1.6 mg cm^{-2}. The electrochemical performance was measured in galvanostatic (dis-)charge experiments, employing a stainless steel 2032 coin cell with lithium metal (Rockwood Lithium, battery grade) as counter electrode. Conversely, CV and EIS measurements of the α-MnS/MnO/SCPF- or α-MnS/MnO-based electrodes were performed in three-electrode cells (Swagelok-type setup) with lithium metal as reference and counter electrodes. In both setups, the WE and lithium metal were separated by a sheet of glass fiber (GF/D, Whatman) as a separator, 1 mol L^{-1} $LiPF_6$ in ethylene carbonate/diethyl carbonate (EC/DEC, 1:1 by volume) solution with 1% (volume) of vinylene carbonate (VC) was used as electrolyte (UBE). The 2032-type coin cells and Swagelok-type cells were assembled in a glove box (MBraun UNIlab; O_2 and H_2O content <0.1 ppm). All electrochemical measurements were carried out at 20 ± 2 °C. The galvanostatic (dis-)charge experiments were performed using a Maccor 3000 battery tester in the voltage range 0.01–3.0 V. CV measurements were conducted with a VMP3 potentiostat (Biologic Science Instruments) in the same potential range, *i.e.*, 0.01–3.0 V *vs.* Li/Li^+. The EIS experiments were performed with the same instrument, in the frequency range from 1 MHz to 10 mHz with a sinusoidal signal amplitude of 5 mV.

In situ XRD measurement

Using a self-designed *in-situ* cell (two-electrode),[3,5] *in situ* XRD analysis of α-MnS/MnO/SCPF was performed upon galvanostatic lithiation and delithiation during the first cycle. The WE slurry with 80 wt% α-MnS/MnO/SCPF, 10 wt% super-C65 and 10 wt% PVdF was cast onto a beryllium (Be) disk (wet thickness of 250 μm). The working electrode was first dried at 60 °C for 3 h and then at 50 °C under vacuum overnight. Lithium foils were used as the counter electrode, while two layers of glass fiber (GF/D, Whatman) soaked with around 300 μL of the electrolyte (1 M $LiPF_6$ in EC/DEC (1/1 volume) added with 1% VC) were employed as separator. The assembled *in-situ* cell was left to rest (at open-circuit voltage) for 12 h before starting the respective experiment. In an experiment, one XRD diffractogram was recorded over a time span of ~30 min, while the *in situ* cell was galvanostatically (dis-)charged using a potentiostat/galvanostat (SP-150, BioLogic) with a specific current of 40 mA g^{-1} and a voltage cut-off of 0.01–3.0 V.

Supporting Information

(see footnote on the first page of this article) Additional references cited with the Supporting Information.[37–52]

Acknowledgements

Y.M. and Y.-J.M. contributed equally to this work. Y.M. Y.-J.M. and K.-C.C. gratefully acknowledge financial support from the Chinese Scholarship Council. Financial support from the Helmholtz Association is also acknowledged. Moreover, the authors would like to thank Dr. Yuanchun Ji for TEM testing and Dr. Damian Goonetilleke for Rietveld refinement analysis. This work contributes to the research performed at CELEST (Center for Electrochemical Energy Storage Ulm-Karlsruhe). Open access funding enabled and organized by Projekt DEAL.

Conflict of Interest

The authors declare no conflict of interest.

Keywords: lithium-ion batteries · heterostructure · α-MnS/MnO nanoparticles · S-doped carbonaceous frameworks · *in situ* XRD/lithium storage mechanism

[1] D. Bresser, S. Passerini, B. Scrosati, *Energy Environ. Sci.* **2016**, *9*, 3348–3367.
[2] X. Gao, B. Wang, Y. Zhang, H. Liu, H. Liu, H. Wu, S. Dou, *Energy Storage Mater.* **2019**, *16*, 46–55.
[3] Y. Ma, Y. Ma, G. Giuli, T. Diemant, R. J. Behm, D. Geiger, U. Kaiser, U. Ulissi, S. Passerini, D. Bresser, *Sustain. Energy Fuels* **2018**, *2*, 2601–2608.
[4] Y. Ma, Y. Ma, D. Bresser, Y. Ji, D. Geiger, U. Kaiser, C. Streb, A. Varzi, S. Passerini, *ACS Nano* **2018**, *12*, 7220–7231.
[5] Y. Ma, Y. Ma, G. Giuli, H. Euchner, A. Groß, G. O. Lepore, F. d'Acapito, D. Geiger, J. Biskupek, U. Kaiser, H. M. Schütz, A. Carlsson, T. Diemant, R. J. Behm, M. Kuenzel, S. Passerini, D. Bresser, *Adv. Energy Mater.* **2020**, *10*, 2000783.
[6] Y. Zhao, L. P. Wang, M. T. Sougrati, Z. Feng, Y. Leconte, A. Fisher, M. Srinivasan, Z. Xu, *Adv. Energy Mater.* **2017**, *7*, 1601424.
[7] Y.-J. Li, C.-Y. Fan, H.-H. Li, K.-C. Huang, J.-P. Zhang, X.-L. Wu, *Chem. Eur. J.* **2018**, *24*, 9606–9611.
[8] Y. Ma, U. Ulissi, D. Bresser, Y. Ma, Y. Ji, S. Passerini, *Electrochim. Acta* **2017**, *258*, 535–543.
[9] G. Zhu, L. Wang, H. Lin, L. Ma, P. Zhao, Y. Hu, T. Chen, R. Chen, Y. Wang, Z. Tie, J. Liu, Z. Jin, *Adv. Funct. Mater.* **2018**, *28*, 1800003.
[10] Y. Ma, Y. Ma, D. Geiger, U. Kaiser, H. Zhang, G.-T. Kim, T. Diemant, R. J. Behm, A. Varzi, S. Passerini, *Nano Energy* **2017**, *42*, 341–352.
[11] Y. Ji, Y. Ma, R. Liu, Y. Ma, K. Cao, U. Kaiser, A. Varzi, Y.-F. Song, S. Passerini, C. Streb, *J. Mater. Chem. A* **2019**, *7*, 13096–13102.
[12] H. Hou, C. E. Banks, M. Jing, Y. Zhang, X. Ji, *Adv. Mater.* **2015**, *27*, 7861–7866.
[13] Y. Zheng, T. Zhou, C. Zhang, J. Mao, H. Liu, Z. Guo, *Angew. Chem. Int. Ed.* **2016**, *55*, 3408–3413; *Angew. Chem.* **2016**, *128*, 3469–3474.
[14] W. Ren, D. Liu, C. Sun, X. Yao, J. Tan, C. Wang, K. Zhao, X. Wang, Q. Li, L. Mai, *Small* **2018**, *14*, 1800659.
[15] Y. Wang, H. Wu, L. Huang, H. Zhao, Z. Liu, X. Chen, H. Liu, Y. Zhang, *Inorg. Chem.* **2018**, *57*, 7993–8001.
[16] K. Chen, X. Kong, X. Xie, J. Chen, X. Cao, S. Liang, A. Pan, *Batteries & Supercaps* **2020**, *3*, 344–353; Supercaps **2020**, 3, 344–353.
[17] Y. Ma, Y. Ma, G. Kim, T. Diemant, R. J. Behm, D. Geiger, U. Kaiser, A. Varzi, S. Passerini, *Adv. Energy Mater.* **2019**, *9*, 1902077.
[18] W. Huang, S. Li, X. Cao, C. Hou, Z. Zhang, J. Feng, L. Ci, P. Si, Q. Chi, *ACS Sustainable Chem. Eng.* **2017**, *5*, 5039–5048.

[19] R. Wu, D. P. Wang, X. Rui, B. Liu, K. Zhou, A. W. K. Law, Q. Yan, J. Wei, Z. Chen, *Adv. Mater.* **2015**, *27*, 3038–3044.
[20] D.-H. Liu, W.-H. Li, Y.-P. Zheng, Z. Cui, X. Yan, D.-S. Liu, J. Wang, Y. Zhang, H.-Y. Lü, F.-Y. Bai, J.-Z. Guo, X.-L. Wu, *Adv. Mater.* **2018**, *30*, 1706317.
[21] J. H. Lee, Y. J. Sa, T. K. Kim, H. R. Moon, S. H. Joo, *J. Mater. Chem. A* **2014**, *2*, 10435–10443.
[22] B. Liu, Z. Liu, D. Li, P. Guo, D. Liu, X. Shang, M. Lv, D. He, *Appl. Surf. Sci.* **2017**, *416*, 858–867.
[23] D. Sun, Y. Tang, D. Ye, J. Yan, H. Zhou, H. Wang, *ACS Appl. Mater. Interfaces* **2017**, *9*, 5254–5262.
[24] F. Zheng, Z. Yin, H. Xia, G. Bai, Y. Zhang, *Chem. Eng. J.* **2017**, *327*, 474–480.
[25] S. J. Yang, S. Nam, T. Kim, J. H. Im, H. Jung, J. H. Kang, S. Wi, B. Park, C. R. Park, *J. Am. Chem. Soc.* **2013**, *135*, 7394–7397.
[26] R. R. Salunkhe, J. Tang, Y. Kamachi, T. Nakato, J. H. Kim, Y. Yamauchi, *ACS Nano* **2015**, *9*, 6288–6296.
[27] H. Su, Y.-F. Xu, S.-C. Feng, Z.-G. Wu, X.-P. Sun, C.-H. Shen, J.-Q. Wang, J.-T. Li, L. Huang, S.-G. Sun, *ACS Appl. Mater. Interfaces* **2015**, *7*, 8488–8494.
[28] Y. Zhang, Y. Yan, X. Wang, G. Li, D. Deng, L. Jiang, C. Shu, C. Wang, *Chem. Eur. J.* **2014**, *20*, 6126–6130.
[29] Z. Cui, Q. Liu, C. Xu, R. Zou, J. Zhang, W. Zhang, G. Guan, J. Hu, Y. Sun, *J. Mater. Chem. A* **2017**, *5*, 21699–21708.
[30] D. Aurbach, Y. Ein-Eli, *J. Electrochem. Soc.* **1995**, *142*, 1746–1752.
[31] B. Liu, Q. Zhang, Z. Jin, L. Zhang, L. Li, Z. Gao, C. Wang, H. Xie, Z. Su, *Adv. Energy Mater.* **2018**, *8*, 1702347.
[32] F. Zheng, M. He, Y. Yang, Q. Chen, *Nanoscale* **2015**, *7*, 3410–3417.
[33] D. Bresser, E. Paillard, P. Niehoff, S. Krueger, F. Mueller, M. Winter, S. Passerini, *ChemPhysChem* **2014**, *15*, 2177–2185.
[34] A. Ponrouch, P.-L. Taberna, P. Simon, M. R. Palacín, *Electrochim. Acta* **2012**, *61*, 13–18.
[35] D. Bresser, E. Paillard, M. Copley, P. Bishop, M. Winter, S. Passerini, *J. Power Sources* **2012**, *219*, 217–222.
[36] C. D. Wanger, D. J. F. Rigga, M. G. E. Moulder, *Handbook of X-ray Photoelectron Spectroscopy*, Perkin-Elmer, Eden Prairie, **1978**.
[37] S. M. Lee, J.-K. Lee, Y. C. Kang, *Chem. Asian J.* **2014**, *9*, 590–595.
[38] D. Chen, H. Quan, Z. Huang, L. Guo, *ChemElectroChem* **2015**, *2*, 1314–1320.
[39] D. Chen, H. Quan, G.-S. Wang, L. Guo, *ChemPlusChem* **2013**, *78*, 843–851.
[40] X. Gu, J. Yue, L. Chen, S. Liu, H. Xu, J. Yang, Y. Qian, X. Zhao, *J. Mater. Chem. A* **2015**, 3, 1037–1041.
[41] N. Zhang, R. Yi, Z. Wang, R. Shi, H. Wang, G. Qiu, X. Liu, *Mater. Chem. Phys.* **2008**, *111*, 13–16.
[42] Y. Hao, C. Chen, X. Yang, G. Xiao, B. Zou, J. Yang, C. Wang, *J. Power Sources* **2017**, *338*, 9–16.
[43] S. Gao, G. Chen, Y. Dall'Agnese, Y. Wei, Z. Gao, Y. Gao, *Chem. Eur. J.* **2018**, *24*, 13535–13539.
[44] J. Ning, D. Zhang, H. Song, X. Chen, J. Zhou, *J. Mater. Chem. A* **2016**, *4*, 12098–12105.
[45] L. Zhang, L. Zhou, H. B. Wu, R. Xu, X. W. D. Lou, *Angew. Chem. Int. Ed.* **2012**, *51*, 7267–7270; *Angew. Chem.* **2012**, *124*, 7379–7382.
[46] F. Zhang, Y. Wang, W. Guo, S. Rao, P. Mao, *Chem. Eng. J.* **2019**, *360*, 1509–1516.
[47] H. Liu, Z. Li, Y. Liang, R. Fu, D. Wu, *Carbon* **2015**, *84*, 419–425.
[48] X. Zhang, Z. Xing, L. Wang, Y. Zhu, Q. Li, J. Liang, Y. Yu, T. Huang, K. Tang, Y. Qian, X. Shen, *J. Mater. Chem.* **2012**, *22*, 17864–17869.
[49] X. Fan, S. Li, L. Lu, *Electrochim. Acta* **2016**, *200*, 152–160.
[50] S. Huang, H. Li, G. Xu, X. Liu, Q. Zhang, L. Yang, J. Cao, X. Wei, *Electrochim. Acta* **2020**, *342*, 136115.
[51] K. Zhong, B. Zhang, S. Luo, W. Wen, H. Li, X. Huang, L. Chen, *J. Power Sources* **2011**, *196*, 6802–6808.
[52] S. Ru, H. Xiao, G. Ma, J. Tan, X. Wang, Z. Ai, *Mater. Lett.* **2020**, *276*, 128244.

Manuscript received: January 24, 2021
Revised manuscript received: February 7, 2021
Accepted manuscript online: February 15, 2021